Title

Numerical simulation of x-ray luminescence optical tomography for small-animal imaging

Journal

Journal of Biomedical Optics, 19(4)

ISSN

1083-3668

Authors

Li, Changqing
Martínez-Dávalos, Arnulfo
Cherry, Simon R

Publication Date

2014-04-02

DOI

10.1117/1.jbo.19.4.046002

Peer reviewed

Numerical simulation of x-ray luminescence optical tomography for small-animal imaging

Changqing Li,[1*] Arnulfo Martinez Davalos,[2] and Simon R. Cherry[3]

[1] School of Engineering, University of California, Merced, Merced CA 95343, USA

[2] Instituto de Física, Universidad Nacional Autónoma de México, A.P. 20-364, 01000 México D.F.

[3] Department of Biomedical Engineering, University of California, Davis, Davis CA 95616, USA

[*] cli32@ucmerced.edu

Revised version submitted to Journal of Biomedical Optics

Feb. 24, 2014

Abstract

X-ray luminescence optical tomography (XLOT) is an emerging hybrid imaging modality in which x-ray excitable particles (phosphor particles) emit optical photons when stimulated with a collimated x-ray beam. XLOT can potentially combine the high sensitivity of optical imaging with the high spatial resolution of x-ray imaging. For reconstruction of XLOT data, we compared two reconstruction algorithms, conventional filtered backprojection (FBP) and a new algorithm, x-ray luminescence optical tomography with excitation priors (XLOT-EP), in which photon propagation is modeled with the diffusion equation and the x-ray beam positions are used as reconstruction priors. Numerical simulations based on dose calculations were used to validate the proposed XLOT imaging system and the reconstruction algorithms. Simulation results showed nanoparticle concentrations reconstructed with XLOT-EP are much less dependent on scan depth than those obtained with FBP. Measurements at just two orthogonal projections are sufficient for XLOT-EP to reconstruct an XLOT image for simple source distributions. The heterogeneity of x-ray energy deposition is included in the XLOT-EP reconstruction and improves the reconstruction accuracy, suggesting that there is a need to calculate the x-ray energy distribution for experimental XLOT imaging.

1. Introduction

Multimodality imaging is increasingly utilized in biomedical applications [1]. Commonly, systems involve the combination of two individual imaging modalities, one a high spatial resolution anatomic modality such as x-ray computed tomography (CT) or magnetic resonance imaging (MRI), the other a high sensitivity functional modality such as positron emission tomography (PET) or fluorescence optical tomography (FOT) [2-6]. Another form of multimodality imaging involves hybrid systems, in which the two imaging modalities interact. One example is photoacoustic tomography (PAT), in which a short pulse laser is used to illuminate tissues generating ultrasound signals [7]. Another example is our proposed technique, x-ray luminescence optical tomography (XLOT), in which collimated x-ray beams excite a contrast agent based on phosphor nanoparticles that emits optical photons which are detected and reconstructed into an image. A related approach has been proposed by Xing and colleagues [8]. XLOT has the potential to simultaneously achieve the high sensitivity of optical imaging and the high spatial resolution of x-ray imaging. Since light has limited penetration depth in biological tissues, XLOT is primarily focused on small-animal imaging, with the goal of providing a new imaging technique to support the needs of researchers developing passive, targeted and activatable nanoparticles for applications in imaging and therapy.

In this paper, numerical simulations of XLOT are used to simulate x-ray excitation of Gd_2O_2S:Eu (GOS) phosphor particles in turbid media by a collimated x-ray beam. The emission of optical photons by the excited GOS and subsequent detection with a sensitive electron multiplying charge-coupled device (EMCCD) camera also is simulated. Importantly, in XLOT, optical emission comes primarily from along the path of the x-ray beam. This information can be incorporated into the reconstruction as an ”excitation prior” thus improving the conditioning

of the inverse problem. Data from the simulated EMCCD measurements are then used to reconstruct the particle concentration distribution with a model-based reconstruction method similar to that used in fluorescence optical tomography [6].

As a high spatial resolution imaging tool, CT is often used to provide anatomical information for PET [3], single photon emission computed tomography (SPECT) [9], and fluorescence optical imaging [10]. Applications of CT in molecular imaging have been limited due to the sensitivity of the technique. By contrast, FOT and bioluminescence optical tomography (BOT) are used in the small-animal molecular imaging field because of their high sensitivity in detecting molecular contrast agents [11,12], but they have limited spatial resolution for deep targets. XLOT has the potential to combine the high sensitivity of FOT/BOT with a spatial resolution that depends on the width of the collimated x-ray beam. An x-ray beam width of 1 mm is readily achieved, and can be maintained virtually independent of the target depth.

Eu^{3+}-doped gadolinium oxysulfide (GOS:) has a high cross-section for diagnostic energy x-rays, excellent light yield and is therefore often the phosphor of choice for x-ray detectors [13]. Nanoscale x-ray excitable particles of GOS and other Eu^{3+}-doped lanthanide compounds have been successfully synthesized [14-18]. It is well known that Eu^{3+} ions in lanthanide compounds emit light in the red region due to $^5D_0 \rightarrow {}^7F_j$ radiative transitions, where j=4 corresponds to emission at wavelengths around 700 nm [18]. This is excellent for in vivo applications due to the low tissue absorption of light at these long wavelengths. GOS is therefore an obvious material to explore for initial XLOT applications. The specific emission spectra of these doped compounds depend on their lattice nature, chemical composition and crystalline structure [18]. Nanostructures of GOS with different shapes and sizes have been reported. Although their

excitation wavelength is blue shifted compared with their bulk counterpart due to quantum confinement effects, the emission wavelengths are the same [17].

X-ray excitable luminescence probes have already been used in scanning x-ray microscopy [19]. A finely focused x-ray beam scanned a sample with x-ray excitable ^{31}P phosphor grains emitting visible photons that were collected by an optical microscope. The microscopic resolution (down to 50 nm) was determined by the x-ray focal spot and not by visible light diffraction limits of ~200 nm. X-ray excitable nanoparticles also are reported in photodynamic activation, especially for deep targets [20]. The x-ray excitable nanoparticles can be coated by an amphiphilic polymer of octylamine-modified poly (acrylic acid) [21] or a plasmonic gold shell to improve the biocompatibility, then functionalized to target antibody-based proteins such as prostate-specific antigen [22]. A plasmonic gold shell has been successfully added on a quantum dot core, still preserving its efficiency [23]. Similarly a plasmonic gold shell could be coated on x-ray excitable nanoparticles, allowing widely studied gold labeling methods to be used with XLOT imaging [24]. The overall concept is that biocompatible phosphor nanoparticles can be used with XLOT as an imaging platform to assist in the preclinical (small-animal) development and optimization of targeted nanoparticles for a broad range of therapeutic and diagnostic purpose, allowing temporal and spatial distribution of these particles to be monitored at high spatial resolution, even deep inside an animal. Other possible applications include monitoring of x-ray radiotherapy enhanced by gold-coated nanoparticles [25] and the development of activatable or environmentally-sensitive XLOT probes in which luminescence is quenched via luminescence resonance energy transfer until the quenching molecules on the particle surface are enzymatically or environmentally modified [26].

The concept of x-ray excitable nanoparticles and their possible application in small-animal imaging was first reported by Carpenter et al. [27]. In these early experiments, it was found that the photon yield was linear with x-ray dose, and the minimum detectable concentration was sub-picomolar for superficial measurements. A prototype imaging system using a charge-coupled device (CCD) camera to detect the x-ray excited particles was proposed. The major differences/innovations in our proposed approach are as follows. *First*, we provide a simultaneous CT imaging system combined with our XLOT implementation. CT can provide anatomical information and surface geometry for quantitative XLOT imaging. *Second*, we propose a model-based reconstruction method for XLOT which can detect deep targets with relatively few measurements thus yielding much shorter measurement time and lower radiation dose. *Third*, we use a collimated x-ray pencil beam with a beam size of about 1 mm in diameter. This can be used to more selectively excite deep targets and achieve higher spatial resolution. It is important to note that XLOT has much higher contrast sensitivity than CT alone. The incremental change in x-ray attenuation in tissue due to introduction of the particles is very small, compared with the attenuation of surrounding tissues, thus the CT scan cannot detect the phosphor particles, even at relatively high concentrations. However the optical background for XLOT imaging is essentially zero, so the contrast from luminescence is very high and low amounts of injected agents can be detected.

In this paper, the feasibility of the proposed XLOT imaging system is studied numerically and a new reconstruction algorithm that incorporates the x-ray information as priors is introduced and evaluated.

2. Materials and Methods

2.1 XLOT imaging system

We simulated a prototype XLOT imaging system with the configuration shown in Fig. 1. The system and experimental results are described in [28]. Briefly, a tungsten target x-ray tube generates x-ray photons up to 80 kVp with a maximum x-ray tube current of 0.25 mA. The x-ray detector has a detection area of 49.2 mm by 49.2 mm and consists of a 1024 by 1024 pixel photodiode array sensor with 48 μm pixel spacing. The x-ray detector is 331 mm away from the x-ray tube. The x-ray beam is collimated with a 5 cm long steel rod having a central through hole of 1 mm diameter. The center of the object being imaged is 248 mm away from the x-ray tube and placed on a motorized rotation stage which in turn is mounted on a motorized linear stage. The collimated x-ray beam scans the object with selectable step number and step pitch, and selectable number of projection angles. The optical photons emitted from phosphor particles within the object are imaged from the top surface of the phantom (see Fig. 1) using an EMCCD camera. All scanning depths described are the distance from the top surface of the phantom.

2.2 X-ray energy spectrum

The X-ray energy spectrum for the simulations was generated using the semiempirical model of Birch and Marshall [29]. First, the unfiltered 70 kVp W spectrum was calculated with the model, then it was filtered with various thicknesses of Al and the resulting spectrum was used to calculate theoretical half-value layer (HVL) curves. These curves were compared with experimental measurements of the HVL performed at three different potentials (50, 60 and 70 kVp), and the additional filtration was adjusted until the theoretical curves matched the experimentally measured ones [30].

2.3 X-ray dose calculation

The number of optical photons emitted from radioluminescent particles when excited by x-ray photons is proportional to the x-ray dose [8]. To simulate physical experiments closely, the absorbed dose distribution for each x-ray beam location at each projection angle was calculated with PENELOPE 2008 [31], a Monte Carlo software package that simulates coupled photon-electron transport in matter at energies down to 1 keV. The x-ray attenuation coefficients of the phantom and the GOS targets are calculated from known attenuation coefficients of their components taking into account the fraction by weight of the different target concentrations. The x-ray tube was set to at 70 kVp and 0.15 mA with an exposure time of 1 second, which corresponds to typical exposure conditions in our laboratory prototype. For each x-ray beam location (corresponding to a single projection line of response through the object), x-ray primary dose, x-ray scatter dose and the x-ray photon distribution on the detector were calculated and recorded.

2.4 Forward modeling for XLOT

We assumed the number of optical photons emitted by phosphor particles within the test object was proportional to the deposited energy (dose) and the particle concentration. Light emission was assumed to be at 703 nm, which is the longest wavelength peak in the emission spectrum of GOS [28]. Optical photon propagation in turbid media such as phantoms or tissues was modeled with the diffusion equation in the continuous wave (CW) domain solved using the finite element method [32]. The cylindrical phantom that was used as a test object was discretized by a finite element mesh with 26615 nodes and 153053 tetrahedral elements. The finite element mesh was generated with Tetgen (Tetgen1.4.1, tetgen.berlios.de). The maximum tetrahedral element volume was 0.5 mm^3. The forward-modeling was implemented in Matlab running on a computer

with 2 2.4 GHz 6-core Intel processors. For numerical phantom studies, we set μ_a and μ_s' to be 0.0126 mm^{-1} and 0.84 mm^{-1}, respectively [6]. In the forward modeling process, the finite element nodes within the target region are assigned as optical photon emitting sources only when they are traversed by an x-ray beam. The source intensity is proportional to the x-ray dose and the concentration of particles. The forward model then computes the number of emitted optical photons that reach the top surface of the phantom to be measured.

2.5 Reconstruction algorithm for XLOT and CT

We propose two reconstruction methods for XLOT. One is the standard filtered backprojection (FBP) method developed for conventional transmission and emission tomography that does not consider optical photon absorption and scattering. The second method is XLOT with excitation priors (XLOT-EP) in which optical photon propagation is modeled with the diffusion equation and the x-ray beam position is added as a spatial prior to constrain the nodes to be reconstructed.

2.5.1 FBP for XLOT: For each rotation angle i and each x-ray beam position j, an EMCCD image of the top surface of the phantom is simulated. The total number of angular projections is I and the number of linear scan locations for each angular projection is J. All pixels on the top surface of the phantom are summed to provide one intensity value M_{ij}. The values of M_{ij} acquired for all x-ray beam positions can be used to form a sinogram (a matrix of the intensity values as a function of the radial offset of the x-ray beam from the center in one direction, versus the projection angle in the other direction). We assume particles have the same quantum yield ε. Each measurement M_{ij} has a line integral,

$$\varepsilon \int C(\bar{r})\, D(\bar{r}) dl = M_{ij} \tag{1}$$

where the line is along the x-ray beam through the object for rotation angle i and linear scan j, $C(\bar{r})$ is the particle concentration and $D(\bar{r})$ the x-ray dose at position $\bar{r}$. A line integral (representing the line along which luminescence is excited by the x-ray pencil beam) is indicated in figure 1 for a particular x-ray beam angle and radial offset. A conventional parallel beam CT FBP algorithm was used to calculate $C(\bar{r})D(\bar{r})$ where $D(\bar{r})$ is assumed constant. In this study, a Shepp-Logan filter with a cut off at the Nyquist frequency was applied.

2.5.2 XLOT-EP for XLOT: XLOT-EP is similar to fluorescence optical tomography (FOT) [33] except that the excitation regions have known locations (along the x-ray beam) and are used as reconstruction priors. The finite element nodes that lie within the x-ray beam region for each x-ray beam location are determined from the CT projection images. The absorption coefficients and the reduced scattering coefficients are known and uniform in this study. The system matrix is calculated as

$$[A] = \begin{bmatrix} \begin{bmatrix} \vec{\Psi}_1 \otimes \vec{\Gamma}_1 \otimes \vec{D}_1 \\ \vdots \\ \vec{\Psi}_{n_d} \otimes \vec{\Gamma}_1 \otimes \vec{D}_1 \end{bmatrix} \\ \vdots \\ \begin{bmatrix} \vec{\Psi}_1 \otimes \vec{\Gamma}_{I\times J} \otimes \vec{D}_{I\times J} \\ \vdots \\ \vec{\Psi}_{n_d} \otimes \vec{\Gamma}_{I\times J} \otimes \vec{D}_{I\times J} \end{bmatrix} \end{bmatrix} \tag{2}$$

in which $\otimes$ denotes the element product of row vectors $\vec{\Psi}_j$, $\vec{\Gamma}_k$ and $\vec{D}_k$ where j is from 1 to n_d and k is from 1 to I×J. n_d is the number of detector nodes on the top surface of the phantom. In this case, unlike FBP, the spatial distribution of the light reaching the phantom surface can be and is incorporated into the reconstruction. The photon fluence vectors, $\vec{\Psi}_{n_d}$, defined on the finite element nodes with dimension of $1 \times n$, are obtained by solving the diffusion equation in the continuous wave (CW) domain,

$$\begin{matrix} -\nabla \cdot \left(D(\lambda)\nabla\Psi_{n_d}\right) + \mu_a(\lambda)\Psi_{n_d} = \Delta_j \\ \vec{n} \cdot \left(D(\lambda)\nabla\Psi_{n_d}\right) + b\Psi_{n_d} = 0 \end{matrix} \quad (3)$$

where ∇ denotes gradient operator, Ψ is optical photon fluence in the turbid media, $\vec{n}$ is the vector normal to the boundary, and b is Robin boundary coefficient. The diffusion coefficient $D(\lambda) = \frac{1}{3\cdot(\mu_s'(\lambda)+\mu_a(\lambda))}$, the reduced scattering coefficients $\mu_s'(\lambda)$ and the absorption coefficients $\mu_a(\lambda)$ are functions of the optical photon wavelength λ. In Eq. 3, Δ_j is determined by the detector nodes. The corresponding node is set to be 1 when Ψ_{n_d} is found by solving Eq. 3 with the finite element method. n is the number of the finite element nodes. The prior constraint vectors $\vec{\Gamma}_k$ (k from 1 to I×J) are calculated as

$$\Gamma_k(m) = \begin{cases} 1 & \text{if node m is within the X} - \text{ray beam} \\ 0 & \text{otherwise} \end{cases} \quad (4)$$

where m runs from 1 to n. The dose distribution vector $\vec{D}_k$ is a row vector representing the x-ray dose distribution calculated with PENELOPE 2008 at each node for each x-ray beam position.

With the calculated system matrix from equation (2), we obtain the linear equation,

$$[A]_{(nd\times I\times J,n)}\,[C]_{(n,1)} = [Y]_{(nd\times I\times J,1)} \quad (5)$$

where $[C]$ is the unknown particle concentration at each node to be reconstructed, and $[Y]$ is the measurement on the top surface of the phantom, obtained from the EMCCD images. In equation (5), the subscripts indicate the dimension of matrices. The preconditioned conjugate gradient (PCG) method is used to reconstruct the particle concentration inside the phantom.

2.5.3 FBP for CT: For each projection i, there are J linear scans. This is equivalent to a parallel beam CT setup with J measurements in each projection. The x-ray beam intensity measurements for each linear scan j at each i, P_{ij}, form a sinogram that is used to reconstruct a CT image by the

conventional FBP reconstruction algorithm. A multiple pixel x-ray detector was used for each P_{ij}. The detector pixels corresponding to the x-ray beam were summed to a single value P_{ij}. In this study, the pencil beam CT image was used to test the x-ray detectability based on attenuation contrast between the target and the phantom background.

2.6 Numerical phantom and scanning parameters

Phantoms that can be produced experimentally and practical scanning procedures that can be realized using the first XLOT prototype scanning system [28] were chosen for the simulation studies.

2.6.1 Phantom Materials and Geometry: A cylindrical phantom (50 mm long and 32 mm in diameter) was simulated with 1% intralipid, 2% agar, 20 μM hemoglobin and with an embedded off-center cylindrical target (4.8 mm diameter, 50 mm long, offset 7.7 mm). The cylindrical target was assumed to be composed of 1% intralipid, 2% agar, 20 μM hemoglobin and GOS powder at different concentrations (10, 1, 0.1 and 0.01 mg/ml).

2.6.2 Numerical Experimental Procedure: For numerical phantom experiments, the phantom was simulated at the center of the stage. For each XLOT scan, the angular step was set at 5 degrees with 36 rotations in total. For each angular step, the linear stage was moved radially in 32 steps with a 1 mm step size. For each distinct x-ray beam position, an image corresponding to the optical photon intensity on the top surface of the phantom was simulated. In addition a pencil beam x-ray projection measuring the x-ray beam attenuation was simulated. The simulated optical images were used to reconstruct XLOT images and the x-ray measurements were used to reconstruct pencil-beam x-ray CT images using the methods described in the previous section.

2.7 Numerical simulation studies

Four different sets of simulations were performed. First, we compared target detectability between CT and XLOT. Second, the two proposed reconstruction methods for XLOT, FBP and XLOT-EP, were compared. Third, we investigated the effects of the number of angular projections on the results using XLOT-EP. Finally, the effects of x-ray scattering and heterogeneous dose distribution on XLOT imaging were studied.

Target Detectability: A visual comparison of target detectability between CT and XLOT for targets with concentrations of 10, 1, 0.1 and 0.01 mg/ml was performed. For both CT and XLOT, the FBP reconstruction method was used. The scan depth (Fig. 1) was set to 10 mm below the top surface of the phantom. 36 projection angles (5° step) with 32 linear steps per angle (1 mm between steps) were simulated for a total of 1,152 measurements. 50% random noise was added to the numerical measurements used in the XLOT reconstruction. The noise to signal ratio was estimated from our experimental measurements [28].

FBP and XLOT-EP: Targets with phosphor concentrations of 10, 1, 0.1 and 0.01 mg/ml were simulated for different scan depths (measured with respect to the top surface of the phantom) with both FBP and XLOT-EP methods. For each concentration, the target was scanned at depths of 5, 10 and 20 mm. The reconstructed concentrations in the target region were compared. For both methods, 36 projection angles (5° step) with 32 linear steps per angle (1 mm between steps) were simulated.

Effect of Number of Projection Angles on XLOT-EP: For one representative case with a phosphor concentration of 1 mg/ml concentration and a scan depth of 5 mm scan, XLOT-EP reconstructions were performed with 1, 2 and 36 angular projections. The one projection

measurement was at 0 degrees (along x axis). The 2 projection measurements were orthogonal at 0 and 90 degrees (along x and y axis).

Effect of X-ray Dose Heterogeneity on XLOT-EP: $\vec{D}_k$ in Eq. 2 indicates that the x-ray dose at each finite element node introduces x-ray dose effects in the XLOT forward modeling and reconstruction. To consider dose heterogeneity in the XLOT reconstruction, $\vec{D}_k$ was set equal to the calculated dose obtained from PENELOPE in simulating the phantom experiments. If the x-ray dose is assumed to be homogeneous throughout the phantom, then $\vec{D}_k$ would equal unity.

X-ray Scattering Effects: The energy deposited from the primary interaction between an x-ray photon and its surrounding medium is the primary dose. The dose from interactions beyond the primary interaction is due to x-ray scattering. For a representative case with a target concentration of 1 mg/ml at a scan depth of 10 mm, two sets of measurements, one generated from total dose including both primary and secondary dose, and another generated from the primary dose only, were used for reconstruction with both FBP and XLOT-EP reconstruction methods. The reconstructed results were analyzed and compared.

3. Results

3.1 X-ray energy spectrum

The computed x-ray energy spectra for 50, 60, and 70 kVp are plotted in Fig. 2. The intensity is given in arbitrary units, and the spectra are renormalized to the value at 20 keV to allow better comparison of their shapes. The attenuation caused by the intrinsic filtration of the x-ray tube has already been included in these spectra and corresponds to 1.3 mm Al. In the following numerical simulations we used the x-ray energy spectrum corresponding to 70 kVp, as shown by the solid line in Fig. 2. The total x-ray fluence for each pencil beam was set to $1x10^5$ x-ray photons, which

corresponds to a tube current of ~0.15 mA for the x-ray tube (SB80250, Oxford Instruments) used in our previous experimental work [28].

3.2 X-ray dose calculation

To simplify the visual presentation of this data, we summed the doses from all 32 linear scan positions for each angular position and show them in Fig. 3 for 6 representative angular projections. The target concentration was set at 10 mg/ml. At this high concentration, the target has high intensity because it absorbs a significant fraction of the incident x-ray energy. The transmitted x-ray photons reach the x-ray detector and their distribution is recorded and used to reconstruct the CT images shown in Fig. 4. The simulated dose distribution for each linear scan position is used to calculate how many optical photons are generated in the target at each location.

3.3 CT images

Simulated pencil-beam CT images reconstructed with FBP are shown in Fig. 4 for phosphor concentrations of 10, 1, 0.1 and 0.01 mg/ml. For concentrations of 10 and 1 mg/ml, the target is detectable in the CT image. For concentrations of 0.1 and 0.01 mg/ml, the target is no longer detectable.

3.4 Forward modeling

For each linear scan at each projection angle, a top surface optical measurement is simulated. For FBP reconstruction of XLOT data, the top surface measurements are integrated and used to form a sinogram (see methods). A typical sinogram for the case of 1 mg/ml concentration and 5 mm scan depth is shown in Fig. 5, with and without x-ray scattering.

3.5 Simulated XLOT images with FBP reconstruction

For all numerical simulation cases, sinograms were generated and used with FBP reconstruction. The reconstructed XLOT images represent particle concentrations in a section at the appropriate scan depth. Reconstructed FBP images are shown in Fig. 6 for a target concentration of 1 mg/ml at a scan depth of 5 mm (a), 10 mm (b), and 20 mm (c). The reconstructed values in the target region vary by an order of magnitude for the same target at different scan depths because optical photon absorption and scattering are not considered in the FBP reconstruction. We only present the FBP reconstruction for measurements using 36 projections. When using FBP reconstruction and only 1 or 2 projections, the target is not detectable.

3.6 XLOT-EP reconstruction with different projections

With XLOT-EP, the x-ray beam position and its spatial extent are applied to the reconstruction algorithm as priors. The optical measurements from the top surface are not summed. Instead, the measured intensity distribution is used. Therefore more information is available in the XLOT-EP algorithm than the FBP algorithm and therefore fewer angular projections may be needed for reconstruction. To demonstrate this, XLOT images were reconstructed with 36 projections, 2 orthogonal projections and 1 projection, respectively. Each angular projection consisted of 32 linear scan positions. Fig. 7 shows the reconstructed images with XLOT-EP for a target concentration of 1 mg/ml and 5 mm irradiation depth using 36 projections (a, b), 2 orthogonal projections (c, d) and just 1 projection (e, f). Two orthogonal projections are sufficient in this case to provide a good reconstructed image. Figs. 7 (a), 7 (c) and 7 (e) assume homogeneous dose. Figs. 7 (b), 7 (d) and 7 (f) consider the dose heterogeneity in reconstruction. We observe that the image quality is slightly better when dose heterogeneity is considered.

Linearity: The reconstructed concentrations in the target region are plotted against the actual concentrations in Fig. 8 for the case of a scan depth of 5 mm. In figure 8(b), the dose heterogeneity is considered for XLOT-EP reconstructions while the dose is assumed to be homogeneous in figure 8 (a). For each plot, the reconstructed values are normalized to that obtained at a concentration of 10 mg/ml and values are shown on a log-log plot. From Fig. 8, we see that the logarithm of the reconstructed concentrations *(log [C_{recon}])* is approximately linearly proportional to the logarithm of the exact concentrations *(log[C_{exact}])*. For the cases in which either two or all 36 projections are used with XLOT-EP, and when heterogenity effects are considered, C_{exact} is linearly proportional to C_{recon} over the entire concentration range studied.

Scan Depth Effects: The maximum concentration in the target region of the reconstructed images was measured and plotted as a function of scan depth for a target concentration of 1 mg/ml (Fig. 9). Ideally, the reconstructed concentrations should be the same at all depths. We calculated the ratio of the reconstructed concentration at 5 mm scan depth to that at 20 mm scan depth. When dose heterogeneity is considered (Fig. 9 (b)), the ratios are 1.06, 1.37, and 2.18 for XLOT-EP images reconstructed with all projections, 2 projections and 1 projection, respectively. The ratio for FBP using all projections is ~180. The XLOT-EP reconstruction using all projections is the least dependent on scanning depth.

Effect of Dose Heterogeneity: For each target concentration and each scan depth, XLOT images were reconstructed with both heterogenous and homogeneous dose distributions. As demonstrated in Fig. 8 and Fig. 9, using the heterogeneous model improves the linearity and reduces the depth dependence of the reconstructed concentration.

Effects of X-ray Scatter: For each numerical simulation case, reconstructions were performed with and without x-ray scatter. No substantial effects were observed, in part because the amount

of x-ray scatter for the relatively small objects of interest for XLOT imaging is low. All results presented above included the effects of x-ray scatter.

4. Discussion and Conclusions

We have explored a novel imaging modality that integrates x-ray excitation with optical detection and offers the prospect of high spatial resolution molecular imaging with much reduced depth dependency. The approach also provides the ability to simultaneously acquire structural CT data. A prototype system has been developed and experimental feasibility established [28]. In this paper, we have used numerical simulations to compare two different approaches to reconstruct XLOT data and have investigated a range of parameters and concerns related with the XLOT, including target detectability, number of projection angles required, dose heterogeneity, linearity, and depth dependence.

The application of CT in molecular imaging has been limited by its low sensitivity. Our simulation results show that CT could not detect the target when the target concentration was less than 1 mg/ml. This is because at low concentrations, the absorption of the target region is not very different from the background region. XLOT takes advantage of the sensitivity of optical detection and the lack of optical background emanating from the background region. Thus XLOT has the potential for much higher sensitivity than CT.

In these numerical studies, we simulate the whole emission and detection process including x-ray absorption and scattering, x-ray excitation, optical photon emission and propagation, and EMCCD measurements. We assume a simple flat 50% random noise model that mainly arises from fluctuations in the x-ray flux and from EMCCD noise. A full noise model for XLOT would also need to include x-ray conversion efficiency and variations in absorbed x-ray energy to optical photons conversion which is complex for materials on the nanometer scale. Furthermore,

precise noise levels heavily depend on the specifics of the optical camera and x-ray tube. For these reasons, a representative noise level is evaluated, although clearly more detailed noise modeling is an important topic for future research.

The FBP method has severe limitations for reconstructing XLOT data as it does not model light propagation, therefore reconstructed target concentrations are strongly depth-dependent. While the reconstructed target size (a surrogate for spatial resolution) is almost the same for targets at different depths using the FBP method, the reconstructed concentration changes 180-fold moving from scan depths of 5 mm to 20 mm. For the proposed XLOT-EP method, the reconstructed target sizes and concentrations are almost independent of depth. For the XLOT-EP method, 2 orthogonal projections are sufficient to reconstruct the target in this simple phantom, although somewhat more dependence on depth is observed. It is likely more complex phantom or source distributions will require additional projections for accurate reconstruction.

XLOT uses high-energy x-ray photons to excite the phosphor particles and therefore has far better penetration depth in terms of excitation than FOT. However, XLOT still measures emitted optical photons, most which are scattered and absorbed when propagating from deep targets to the surface where they are measured. XLOT therefore can likely image deeper than FOT but will still have limited penetration depth compared to CT. Any comparison with FOT, however, is highly situation-dependent, as the wavelengths used and the optical properties of the relevant tissues at those wavelengths will determine the depth that can be achieved with either technique.

In summary, we have proposed an XLOT imaging system to detect light from particles that display x-ray luminescence and that are embedded in a turbid, tissue-like media. A simultaneous pencil beam CT system is combined into the XLOT system. We have compared two reconstruction methods for XLOT, FBP and XLOT-EP using numerical simulations with

different GOS concentrations in target. Simulation results have shown that the reconstructed concentrations with XLOT-EP are much less dependent on the scan depths than with FBP. Measurements using two orthogonal projections are enough to reconstruct an XLOT image of this simple phantom geometry with XLOT-EP although depth-dependence is slightly increased. The reconstructed concentrations from XLOT-EP are linear with the actual concentrations over a wide range. The x-ray dose is heterogeneously distributed in phantoms and the inclusion of the heterogeneity into XLOT reconstruction improves the quantitative accuracy of the reconstructed images.

Now that first imaging instrumentation and reconstruction methodology for XLOT has become available, future development of the technique depends on the availability of biocompatible phosphor nanoparticles that can be administered as contrast agents in vivo. Several efforts are currently underway to develop these agents [34-36].

ACKNOWLEDGMENT

This work was funded in part by grant R21 EB013828 from the National Institutes of Health.

REFERENCES:

1. S. R. Cherry, "Multimodality in vivo imaging systems: Twice the power or double the trouble?" Annu. Rev. Biomed. Eng. **8,** 35-62 (2006).
2. D. W. Townsend, "Multimodality imaging of structure and function," Phys. Med. Biol. **53,** R1-R39 (2008).
3. H. Liang, Y. Yang, K. Yang, Y. Wu, J. Boone, and S. Cherry, "A microPET/CT system for in vivo small animal imaging," Phys. Med. Biol. **52,** 3881 (2007).

4. C. Catana, D. Procissi, Y. B. Wu, M. S. Judenhofer, J. Y. Qi, B. J. Pichler, R. E. Jacobs, and S. R. Cherry, "Simultaneous in vivo positron emission tomography and magnetic resonance imaging," Proc. Natl. Acad. Sci. **105,** 3705-3710 (2008).
5. V. Ntziachristos, A. G. Yodh, M. Schnall, and B. Chance, "Concurrent MRI and diffuse optical tomography of breast after indocyanine green enhancement," Proc. Natl. Acad. Sci. **97,** 2767-2772 (2000).
6. C. Li, G. S. Mitchell, J. Dutta, S. Ahn, R. M. Leahy, and S. R. Cherry, "A three-dimensional multispectral fluorescence optical tomography imaging system for small animals based on a conical mirror design," Optics Express **17,** 7571-7585 (2009).
7. X. D. Wang, Y. J. Pang, G. Ku, X. Y. Xie, G. Stoica, and L. H. V. Wang, "Noninvasive laser-induced photoacoustic tomography for structural and functional in vivo imaging of the brain," Nat. Biotechnol. **21,** 803-806 (2003).
8. G. Pratx, C. M. Carpenter, C. Sun, and L. Xing, "X-Ray Luminescence Computed Tomography via Selective Excitation: A Feasibility Study," IEEE Trans. Med. Imaging **29,** 1992-1999 (2010).
9. K. LaCroix, B. Tsui, B. Hasegawa, and J. Brown, "Investigation of the use of X-ray CT images for attenuation compensation in SPECT," IEEE Trans. Nucl. Sci. **41,** 2793-2799 (1994).
10. R. B. Schulz, A. Ale, A. Sarantopoulos, M. Freyer, E. Soehngen, M. Zientkowska, and V. Ntziachristos, "Hybrid system for simultaneous fluorescence and x-ray computed tomography," IEEE Trans. Med. Imag. **29,** 465-473 (2010).

11. V. Ntziachristos, J. Ripoll, L. V. Wang, and R. Weissleder, "Looking and listening to light: the evolution of whole-body photonic imaging," Nat. Biotechnol. **23,** 313-320 (2005).

12. G. Wang, W. X. Cong, K. Durairaj, X. Qian, H. Shen, P. Sinn, E. Hoffman, G. McLennan, and M. Henry, "In vivo mouse studies with bioluminescence tomography," Optics Express **14,** 7801-7809 (2006).

13. M. Gambaccini, A. Taibi, A. DelGuerra, M. Marziani, and A. Tuffanelli, "MTF evaluation of a phosphor-coated CCD for x-ray imaging," Phys. Med. Biol. **41,** 2799-2806 (1996).

14. H. Wang, R. Wang, X. Sun, R. Yan, and Y. Li, "Synthesis of red-luminescent Eu^{3+}-doped lanthanides compounds hollow spheres," Mater. Res. Bull. **40,** 911-919 (2005).

15. Y. Tian, W. H. Cao, X. X. Luo, and Y. Fu, "Preparation and luminescence property of Gd_2O_2S : Tb X-ray nano-phosphors using the complex precipitation method," J. Alloys Compounds **433,** 313-317 (2007).

16. M. M. Xing, W. H. Cao, T. Pang, X. Q. Ling, and N. Chen, "Preparation and characterization of monodisperse spherical particles of X-ray nano-phosphors based on Gd_2O_2S:Tb," Chinese Sci. Bull. **54,** 2982-2986 (2009).

17. J. Thirumalai, R. Chandramohan, S. Valanarasu, T. A. Vijayan, R. M. Somasundaram, T. Mahalingam, and S. R. Srikumar, "Shape-selective synthesis and opto-electronic properties of Eu^{3+}-doped gadolinium oxysulfide nanostructures," J. Mater. Sci. **44,** 3889-3899 (2009).

18. A. M. Pires, M. R. Davolos, and E. B. Stucchi, "Eu^{3+} as a spectroscopic probe in phosphors based on spherical fine particle gadolinium compounds," Int. J. Inorg. Mater. **3,** 785-790 (2001).

19. C. Jacobsen, S. Lindaas, S. Williams, and X. Zhang, "Scanning luminescence x-ray microscopy - imaging fluorescence dyes at suboptical resolution," J. Microsc-Oxford **172,** 121-129 (1993).

20. Y. F. Liu, W. Chen, S. P. Wang, and A. G. Joly, "Investigation of water-soluble x-ray luminescence nanoparticles for photodynamic activation," Appl. Phys. Lett. **92,** 43901-43903 (2008).

21. S. Wang, B. R. Jarrett, S. M. Kauzlarich, and A. Y. Louie, "Core/shell quantum dots with high relaxivity and photoluminescence for multimodality imaging," J. Am. Chem. Soc. **129,** 3848-3856 (2007).

22. B. Lutz, C. Dentinger, L. Sun, L. Nguyen, J. Zhang, A. Chmura, A. Allen, S. Chan, and B. Knudsen, "Raman nanoparticle probes for antibody-based protein detection in tissues," J. Histochem. Cytochem. **56,** 371-379 (2008).

23. Y. Jin and X. Gao, "Plasmonic fluorescent quantum dots," Nature nanotechnology **4,** 571-576 (2009).

24. J. F. Hainfeld and R. D. Powell, "New frontiers in gold labeling," J. Histochem. Cytochem. **48,** 471-480 (2000).

25. J. F. Hainfeld, D. N. Slatkin, and H. M. Smilowitz, "The use of gold nanoparticles to enhance radiotherapy in mice," Phys. Med. Biol. **49,** N309 (2004).

26. M. Ogawa, N. Kosaka, M. R. Longmire, Y. Urano, P. L. Choyke, and H. Kobayashi, "Fluorophore− quencher based activatable targeted optical probes for detecting in vivo cancer metastases," Mol. pharmaceutics **6,** 386-395 (2009).

27. C. M. Carpenter, C. Sun, G. Pratx, R. Rao, and L. Xing, "Hybrid x-ray/optical luminescence imaging: Characterization of experimental conditions," Med. Phys. **37,** 4011-4011 (2010).

28. C. Li, K. Di, J. Bec, and S. R. Cherry, "X-ray luminescence optical tomography imaging: experimental studies," Opt. Lett. **38,** 2339-2341 (2013).

29. R. Birch and M. Marshall, "Computation of bremsstrahlung x-ray-spectra and comparison with spectra measured with a ge(li) detector," Phys. Med. Biol. **24,** 505-517 (1979).

30. A. Martinez-Davalos, C. Li, M. Rodriguez-Villafuerte, and S. R. Cherry,"Dosimetric characterization of an x-ray luminescence optical tomography scanner prototype", presented at the *IEEE Nuclear Science Symposium and Medical Imaging Conference, Valencia, Spain, 23-29*, Oct. 2011.

31. F. Salvat, J. Fernandez-Varea, and J. Sempau, "PENELOPE-2008: A code system for Monte Carlo simulation of electron and photon transport," in *Workshop Proceedings* (Barcelona, Spain, Jun. 30 to Jul. 3, 2008), NEA 6416.

32. KD Paulsen, HB Jiang, "Spatially varying optical property reconstruction using a finite element diffusion equation approximation", Med. Phys. 22, 691-701, 1995.

33. C. Li, G. Wang, J. Qi, and S. R. Cherry, "Three-dimensional fluorescence optical tomography in small-animal imaging using simultaneous positron-emission-tomography priors," Opt. Lett. **34,** 2933-2935 (2009).

34. C. Sun, G. Pratx, C. M. Carpenter, H. Liu, Z. Cheng, S. S. Gambhir, L. Xing, "Synthesis and radioluminescence of PEGylated Eu^{3+}-doped nanophosphors as bioimaging probes", Adv. Mater. 23, H195-H199, 2011.

35. L. Sudheendra, G. K. Das, C. Li, S. R. Cherry, and I. M. Kennedy,"Lanthanide-doped nanoparticles for hybrid x-ray/optical imaging" in *Proceeding of SPIE, (BiOS*, San Francisco, CA, 2013), 85960D-8.

36. L. Sudheendra, G. K. Das, C. Li, D. Stark, J. Cena, S. R. Cherry, and I. M. Kennedy,"$NaGdF_4:Eu^{3+}$ nanoparticles for enhanced X-ray optical imaging", Chemistry of Materials (In press, 2014).

Author Biographies:

Changqing Li is an Assistant Professor in School of Engineering, University of California Merced. He received his Ph.D. from Department of Biomedical Engineering, University of Florida in 2006. His research interests are in the fields of preclinical and clinical biomedical imaging, such as diffuse optical tomography, fluorescence molecular tomography, and Cerenkov imaging.

Arnulfo Martínez Dávalos, Ph.D.; Associate Professor. Dr. Arnulfo Martínez Dávalos received his Ph.D. in Radiation Physics from the Department of Medical Physics and Bioengineering of University College London, UK. He joined the faculty of Instituto de Física UNAM in 1995. His main scientific interests are the Monte Carlo simulation of radiation transport in matter, the design and development of ionizing radiation detectors, and its application in Medical Physics and High Energy Physics.

Simon R. Cherry is a Professor in the Departments of Biomedical Engineering and Radiology, and Director of the Center for Molecular and Genomic Imaging, at the University of California, Davis. He holds a Ph.D. in Medical Physics from the University of London. His research interests are in the field of in vivo molecular imaging.

FIGURE CAPTIONS:

Fig. 1. Schematic drawing of the prototype XLOT imaging system that was simulated.

Fig. 2. Simulated x-ray photon energy spectra. The 70 kVp spectrum (solid line) was used for the simulations presented in this paper.

Fig. 3. The dose distribution (sum of all linear steps) for different projection angles at a target concentration of 10 mg/ml. Color indicates the normalized x-ray dose in arbitrary units.

Fig. 4. CT images reconstructed with FBP for target concentrations of 10, 1, 0.1 and 0.01 mg/ml. Because of the relative insensitivity of x-ray contrast, only the higher concentrations can be detected. All images are scaled to a common maximum, intensity corresponds to reconstructed pixel values in arbitrary units.

Fig. 5. The XLOT sinogram (integration of optical photons reaching top surface of phantom for each x-ray beam position) for a target with a concentration of 1 mg/ml and for a scan depth of 5 mm. Top row (no scattering), bottom row (including x-ray scatter). The intensities on the right are shown on a logarithmic scale to allow the effects of x-ray scatter to be better appreciated.

Fig. 6. XLOT images reconstructed with FBP for a target concentration of 1 mg/ml at depths of 5 mm (a), 10 mm (b), and 20 mm (c). X-ray scattering is included in the simulation.

Fig. 7. For target concentrations of 1 mg/ml and 5 mm irradiation depth, images reconstructed with XLOT-EP using 36 angular projections (a, b), 2 orthogonal projections (c, d) and 1 projection (e, f). Left column images (a, c, e) assume a uniform dose distribution and right column images (b, d, f) include the dose heterogeneity in the reconstruction. X-ray scattering is included in the simulations.

Fig. 8. Reconstructed concentration (normalized) versus actual target concentration for 5 mm scan depth for the two reconstruction methods and for different number of projection angles for

XLOT-EP reconstruction. Figure (a) assumes homogeneous dose distribution. XLOT-EP reconstruction in figure (b) considers dose heterogeneity. X-ray scattering is included in both plots. Plots are on a logarithmic scale.

Fig. 9. Reconstructed concentration versus scan depth (normalized to results at 5 mm scan depth). XLOT-EP reconstruction in figure (a) assumes homogeneous dose distribution. Figure (b) considers dose heterogeneity.

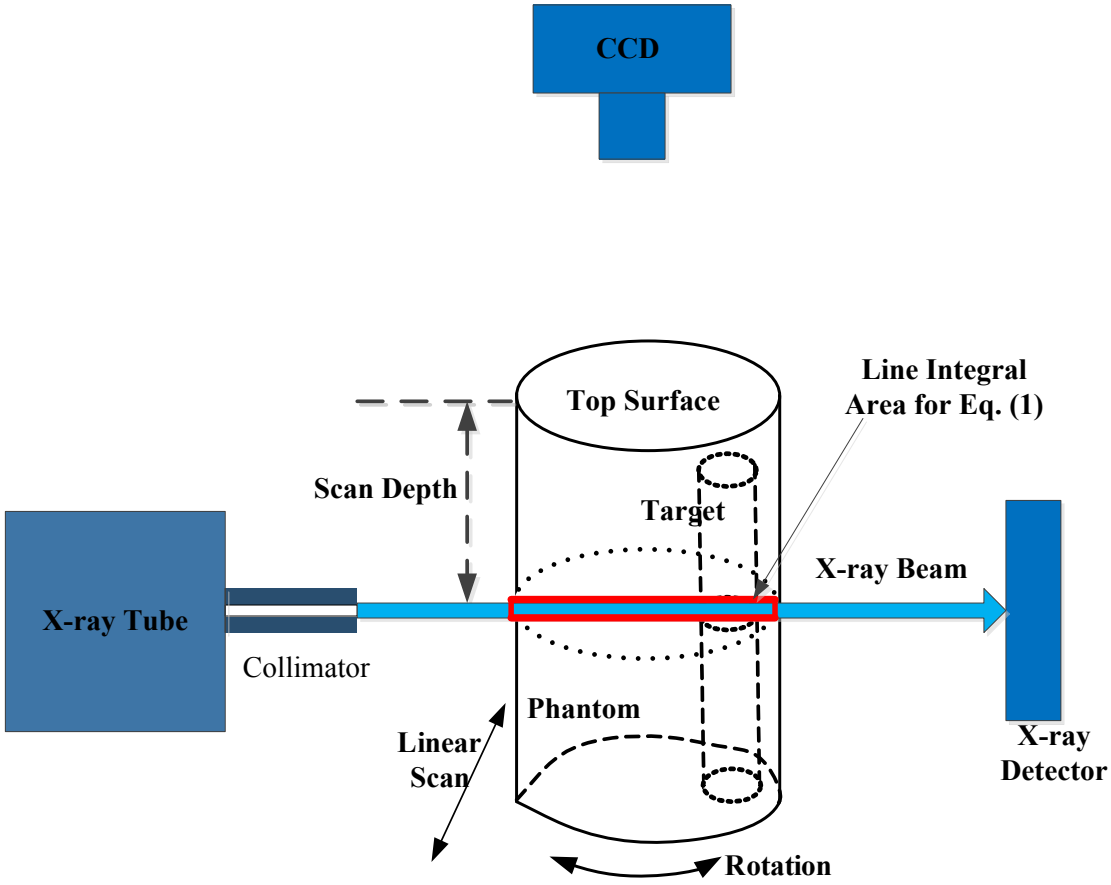
CCD
Top Surface
Line Integral
Area for Eq. (1)
Scan Depth
Target
X-ray Beam
X-ray Tube
Collimator
Phantom
Linear
Scan
X-ray
Detector
Rotation

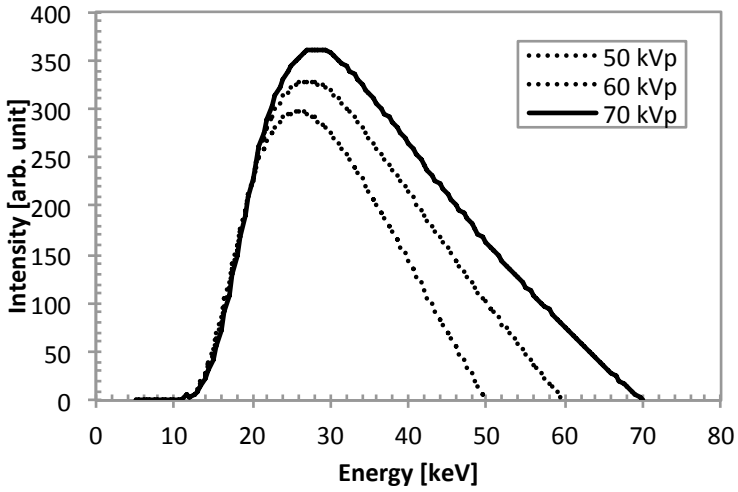
400
350
300
250
200
150
100
50
0
Intensity [arb. unit]
0
10
20
30
40
50
60
70
80
Energy [keV]
50 kVp
60 kVp
70 kVp

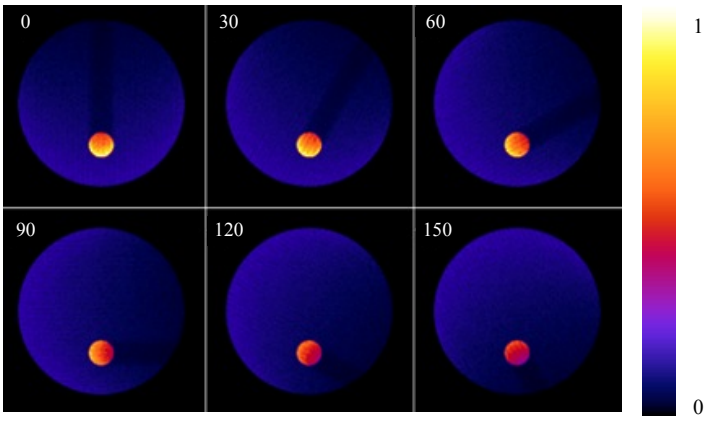
0
30
60
90
120
150
1
0

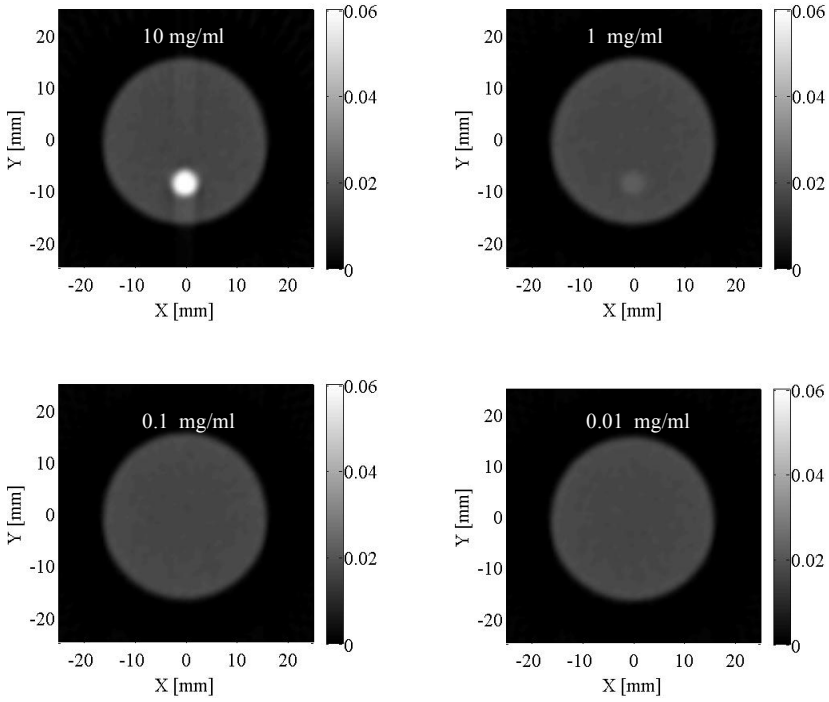
10 mg/ml
1 mg/ml
0.1 mg/ml
0.01 mg/ml
Y [mm]
X [mm]
20
10
0
-10
-20
-20 -10 0 10 20
0.06
0.04
0.02
0

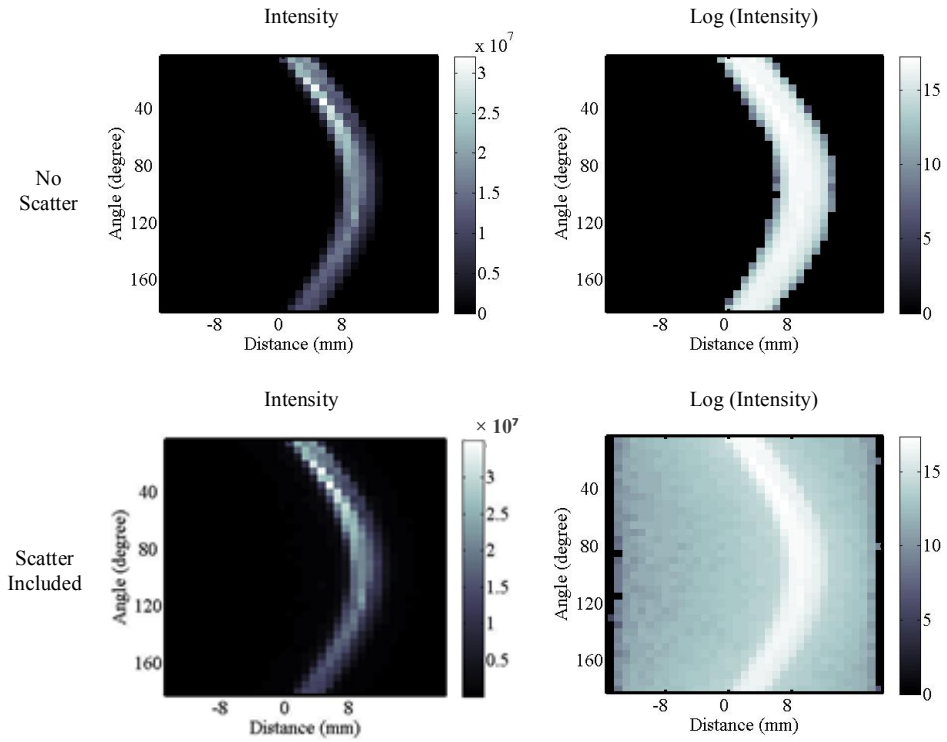
Intensity
Log (Intensity)
No Scatter
Scatter Included
x 10^7
Angle (degree)
Distance (mm)
40
80
120
160
-8
0
8
3
2.5
2
1.5
1
0.5
0
15
10
5

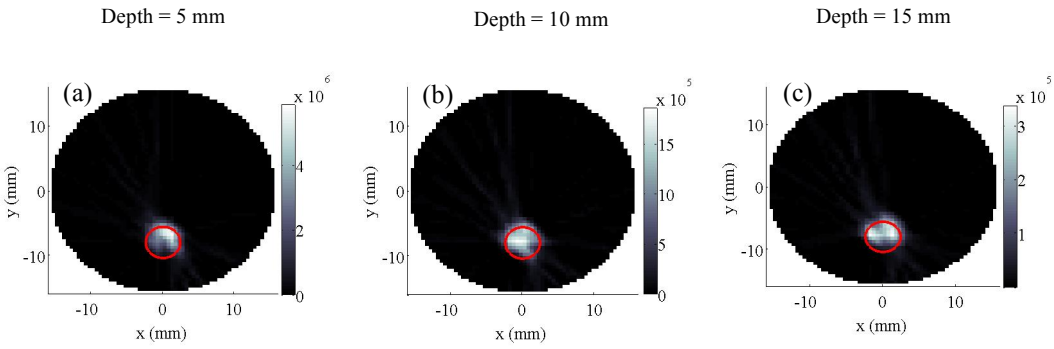
Depth = 5 mm
Depth = 10 mm
Depth = 15 mm
(a)
(b)
(c)
x 10^6
x 10^5
x 10^5
y (mm)
x (mm)
10
0
-10
4
2
15
5
3
1

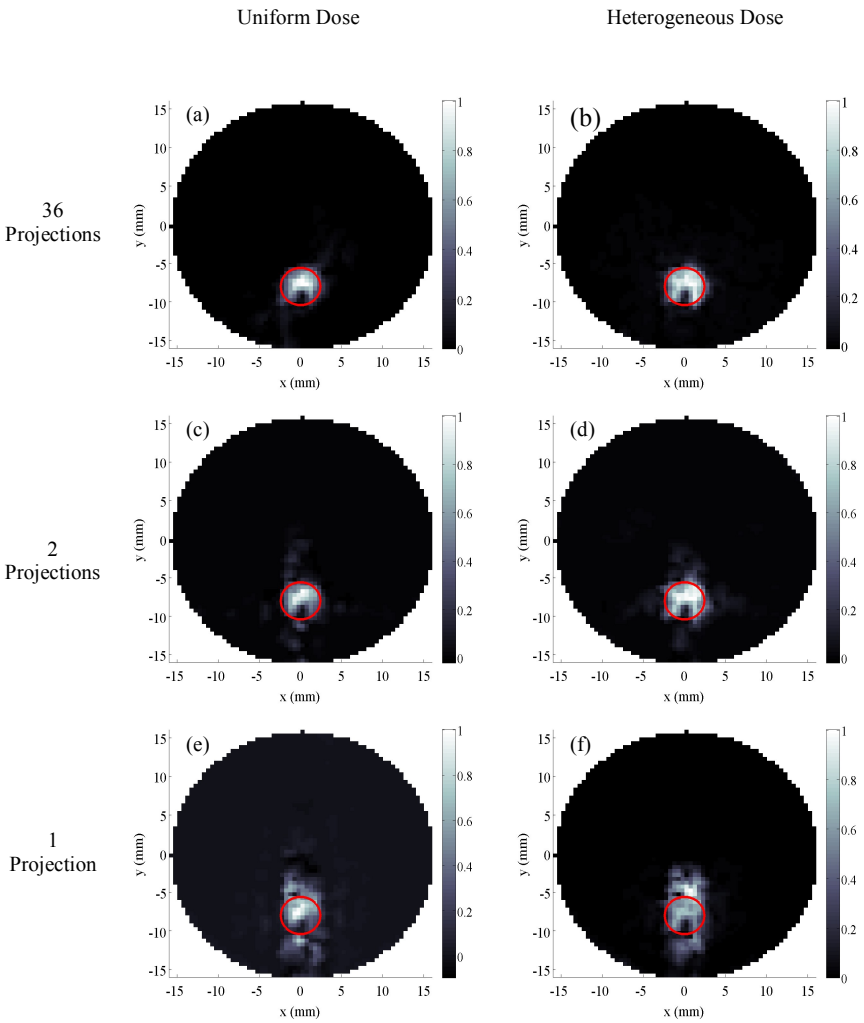
Uniform Dose
Heterogeneous Dose
36 Projections
2 Projections
1 Projection
(a)
(b)
(c)
(d)
(e)
(f)
x (mm)
y (mm)

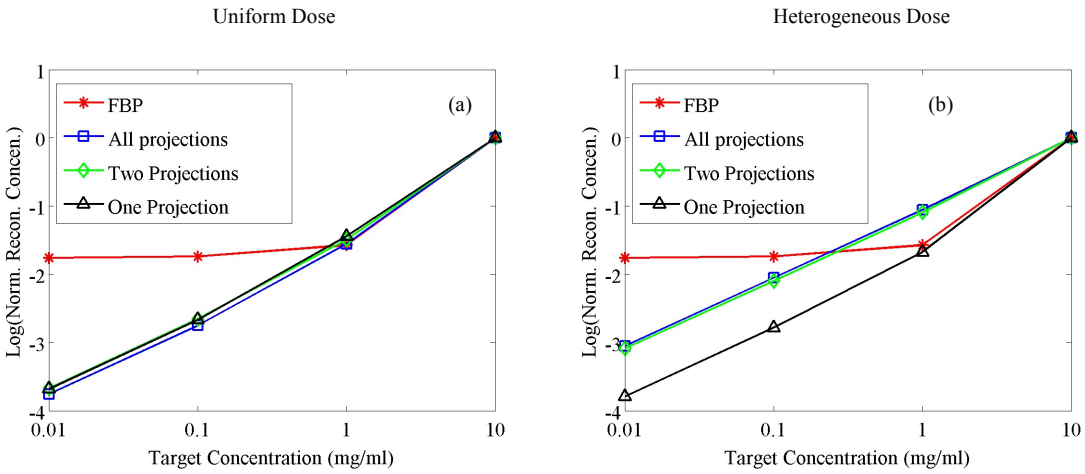
Uniform Dose
Heterogeneous Dose
FBP
All projections
Two Projections
One Projection
(a)
(b)
Log(Norm. Recon. Concen.)
Target Concentration (mg/ml)
1
0
-1
-2
-3
-4
0.01
0.1
1
10

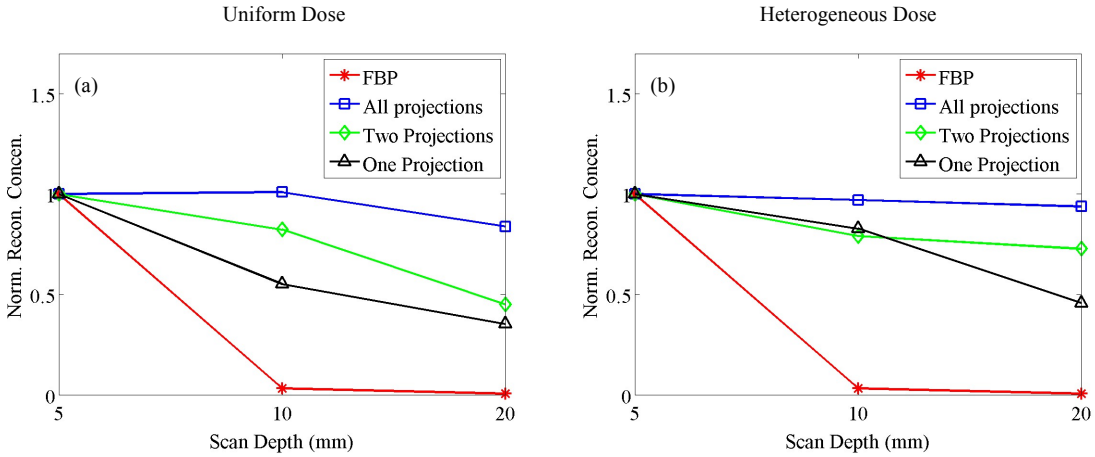
Uniform Dose
Heterogeneous Dose
(a)
(b)
FBP
All projections
Two Projections
One Projection
Norm. Recon. Concen.
Scan Depth (mm)
0
0.5
1
1.5
5
10
20